

1 **Variability of vertical structure of precipitation with sea surface temperature over the**
2 **Arabian Sea and the Bay of Bengal as inferred by TRMM PR measurements**

3 **Kadiri Saikranthi¹, Basivi Radhakrishna², Thota Narayana Rao² and**

4 **Sreedharan Krishnakumari Satheesh³**

5 ¹ *Department of Earth and Climate Science, Indian Institute of Science Education and*
6 *Research (IISER), Tirupati, India.*

7 ² *National Atmospheric Research Laboratory, Department of Space, Govt. of India, Gadanki*
8 *- 517112, India.*

9 ³ *Divecha Centre for Climate Change, Centre for Atmospheric and Oceanic Sciences, Indian*
10 *Institute of Science, Bangalore - 560012, India.*

11

12

13

14

15

16

17

18

19

20

21

22

23

24

25

26

27

28

29

30 **Address of the corresponding author**

31 Dr. K. Saikranthi,

32 Department of Earth and Climate Science,

33 Indian Institute of Science Education and Research (IISER),

34 Tirupati,

35 Andhra Pradesh, India.

36 Email: ksaikranthi@gmail.com

37 **Abstract**

38 Tropical rainfall measuring mission precipitation radar measurements are used to
39 examine the variation of vertical structure of precipitation with sea surface temperature (SST)
40 over the Arabian Sea (AS) and Bay of Bengal (BOB). The variation of reflectivity and
41 precipitation echo top with SST is remarkable over the AS but small over the BOB. The
42 reflectivity increases with SST (from 26°C to 31°C) by ~1 dBZ and 4 dBZ above and below
43 6 km, respectively, over the AS while, its variation is < 0.5 dBZ over the BOB. The
44 transition from shallow storms at lower SSTs ($\leq 27^\circ\text{C}$) to deeper storms at higher SSTs is
45 strongly associated with the decrease in stability and mid-tropospheric wind shear over the
46 AS. Contrary, the storms are deeper at all SSTs over the BOB due to weaker stability and
47 mid-tropospheric wind shear. At lower SSTs, the observed high aerosol optical depth (AOD)
48 and low total column water vapor (TCWV) over AS results in small cloud effective radius
49 (CER) and weaker reflectivity. As SST increases, AOD decreases and TCWV increases
50 leading to large CER and high reflectivity. The changes in these parameters with SST are
51 marginal over the BOB and hence the CER and reflectivity. The predominance of collision-
52 coalescence process below the bright band is responsible for the observed negative slopes in
53 the reflectivity over both the seas. The observed variations in reflectivity are originated at the
54 cloud formation stage over both the seas and these variations are magnified during the
55 descent of hydrometeors to ground.

56

57

58

59

60

61

62

63 **1. Introduction**

64 Indian summer monsoon (ISM - June through September) is one of the most complex
65 weather phenomena, involving coupling between the atmosphere, land and ocean. At the
66 boundary of the ocean and atmosphere air-sea interactions play a key role for the coupled
67 Earth system (Wu and Kirtman 2005; Feng et al. 2018). The sea surface temperature (SST) –
68 precipitation relations are the important measures for the air-sea interactions on different
69 temporal scales (Woolnough et al., 2000; Rajendran et al. 2012). Recent studies (Wang et al.
70 2005; Rajeevan et al. 2012; Chaudhari et al. 2013; 2016; Weller et al. 2016; Feng et al. 2018)
71 have shown that the simulation of ISM can be improved with the exact representation of SST
72 - precipitation relationship. SST modulates the meteorological factors that influence the
73 formation and evolution of different kinds of precipitating systems over tropical oceans
74 (Gadgil et al. 1984; Schumacher and Houze, 2003; Takayabu et al. 2010; Oueslati and Bellon
75 2015).

76 The studies dealing with SST and cloud/precipitation population considered whole
77 Indian Ocean as a single entity (Gadgil et al. 1984; Woolnough et al., 2000; Rajendran et al.
78 2012; Sabin et al. 2012; Meenu et al. 2012; Nair and Rajeev 2014; Roxy 2014). But in reality
79 the Bay of Bengal (BOB) and the Arabian Sea (AS) of Indian Ocean possess distinctly
80 different features. The monsoon experiment (MONEX) and Bay of Bengal monsoon
81 experiment (BOBMEX) have shown how these two seas are different with respect to each
82 other, in terms of SST, back ground atmosphere and the occurrence of precipitating systems
83 (Krishnamurti 1985; Houze and Churchill 1987; Gadgil 2000; Bhat et al. 2001). The SST in
84 the AS cools between 10 °N and 20 °N during the monsoon season whereas warming is seen
85 in other global Oceans between the same latitudes (Krishnamurthi 1981). SST variability is
86 large over the AS than the BOB at seasonal and intraseasonal scales (Sengupta et al. 2001;
87 Roxy et al. 2013). The monsoonal winds (in particular the low-level jet) are stronger over the

88 AS than BOB (Findlater 1969). Also, lower-tropospheric thermal inversions are more
89 frequent and stronger over the AS than BOB (Narayanan and Rao 1981; Sathiyamoorthy et
90 al. 2013). Thus, the atmospheric and sea surface conditions and in turn the occurrence of
91 different kinds of precipitating systems are quite different over the BOB and the AS during
92 the ISM period. For instance, long-term measurements of tropical rainfall measuring mission
93 (TRMM) precipitation radar (PR) have shown that shallow systems are more prevalent over
94 the AS, while deeper systems occur frequently over the BOB (Liu et al. 2007; Romatschke et
95 al. 2010; Saikranthi et al. 2014, 2018; Houze et al. 2015).

96 The aforementioned studies mainly focused on the morphology of vertical structure of
97 precipitation, but, none of them studied the variation of vertical structure of precipitation (in
98 terms of occurrence and intensity) with SST and the differences in the vertical structure over
99 AS and BOB. On the other hand, information on the vertical structure of precipitation is
100 essential for improving the accuracy of rainfall estimation (Fu and Liu 2001; Sunilkumar et
101 al. 2015), understanding the dynamical and microphysical processes of hydrometeor
102 growth/decay mechanisms (Houze 2004; Greetz and Dejene 2005; Saikranthi et al. 2014; Rao
103 et al. 2016) and for improving the latent heating retrievals (Tao et al. 2006). SST being the
104 main driving force to trigger precipitating systems through air-sea interactions (Sabin et al.
105 2012; Nuijens et al. 2017), can alter the vertical structure of precipitation (Oueslati and
106 Bellon 2015). Therefore, the present study aims to understand the variation of vertical
107 structure of precipitation (in terms of precipitation top height and intensity) with SST over the
108 AS and BOB. Besides the SST, vertical structure can be modified by aerosols (or CCN,
109 mostly at the cloud formation stage) and thermodynamics of the ambient atmosphere. For
110 instance, recent studies have shown the impact of surface PM_{10} aerosols in altering the
111 vertical structure of precipitation (Guo et al., 2018). All these parameters, therefore, are
112 considered in the present study to explain the differences in the vertical structure.

113 2. Data

114 The present study utilizes 16 years (1998-2013) of TRMM-PR's 2A25 (version 7)
115 dataset, comprising of vertical profiles of attenuation corrected reflectivity (Iguchi et al.
116 2009), during the ISM. The range resolution of TRMM-PR reflectivity profiles is 250 m with
117 a horizontal footprint size of ~4.3 and 5 km before and after the boosting of its orbit from 350
118 km to 403 km, respectively. It scans $\pm 17^\circ$ from nadir with a beam width of 0.71° covering a
119 swath of 215 km (245 km after the boost). The uniqueness of TRMM-PR data is its ability in
120 pigeonholing the precipitating systems into convective, stratiform and shallow rain. This
121 classification is based on two methods namely the horizontal method (H - method) and the
122 vertical method (V - method) (Awaka et al. 2009). The original TRMM-PR 2A25 vertical
123 profiles of attenuation corrected reflectivity are gridded to a three dimensional Cartesian
124 coordinate system with a spatial resolution of $0.05^\circ \times 0.05^\circ$. The detailed methodology of
125 interpolating the TRMM-PR reflectivity data into the 3D Cartesian grid is discussed in Houze
126 et al. (2007). This dataset is available at the University of Washington website
127 (<http://trmm.atmos.washington.edu/>).

128 To understand the observed variations in the vertical structure of precipitation in the
129 light of microphysics of clouds, Moderate Resolution Imaging Spectroradiometer (MODIS)
130 AQUA satellite level 3 data (MYD08) are considered. In particular, the daily atmospheric
131 products of aerosol optical depth (AOD) (Hubanks et al. 2008) and cloud effective radius
132 (CER) liquid (Platnick et al. 2017) during the period 2003 and 2013 have been used. MODIS
133 AOD dataset is a collection of aerosol optical properties at 550 nm wavelength, as well as
134 particle size information. Level 2 MODIS AOD is derived from radiances using either one of
135 the three different algorithms, i.e., over ocean Remer et al. (2005) algorithm, over land the
136 Dark-Target (Levy et al. 2007) algorithm and for brighter land surfaces the Deep-Blue (Hsu
137 et al. 2004) algorithm. CER is nothing but the weighted mean of the size distribution of cloud

138 drops i.e., the ratio of third moment to second moment of the drop size distribution. In the
 139 level 3 MODIS daily dataset, aerosol and cloud products of level 2 data pixels with valid
 140 retrievals within a calendar day are first aggregated and gridded to a daily average with a
 141 spatial resolution of $1^\circ \times 1^\circ$. For CER grid box values, CER values are weighted by the
 142 respective ice/liquid water cloud pixel counts for the spatiotemporal aggregation and
 143 averaging processes.

144 The background atmospheric structure (winds and total column water vapor) and SST
 145 information are taken from the European Centre for Medium Range Weather Forecasting
 146 (ECMWF) Interim Reanalysis (ERA) (Dee et al. 2011). ERA-Interim runs 4DVAR
 147 assimilation twice daily (00 and 12 UTC) to determine the most likely state of the atmosphere
 148 at a given time (analysis). The consistency across variables in space and time (during 12-hour
 149 intervals) is thus ensured by the atmospheric model and its error characteristics as specified in
 150 the assimilation. ERA-Interim is produced at T255 spectral resolution (about 0.75° , ~ 83 km)
 151 with a temporal resolution of 6h for upper air fields and 3h for surface fields. The original
 152 $0.75^\circ \times 0.75^\circ$ spatial resolution gridded dataset is rescaled to a resolution of $0.125^\circ \times 0.125^\circ$.
 153 The temporal resolution of the dataset used in the present study is 6h (00, 06, 12 and 18
 154 UTC). The equivalent potential temperature (θ_e) is estimated from the ERA-Interim datasets
 155 using the following formula (Wallace and Hobbs 2006):

$$\theta_e = \theta \exp\left(\frac{L_v w_s}{C_p T}\right) \quad (1)$$

156 where θ is the potential temperature, L_v is the latent heat of vaporization, w_s is the saturation
 157 mixing ratio, C_p is the specific heat at constant pressure and T is the absolute temperature.

158 The variation of vertical structure of precipitation with SST are studied by considering
 159 the dataset between $63^\circ\text{E} - 72^\circ\text{E}$ and $8^\circ\text{N} - 20^\circ\text{N}$ over the AS and $83^\circ\text{E} - 92^\circ\text{E}$ and 8°N
 160 $- 21^\circ\text{N}$ over the BOB. These regions of interest along with the ISM seasonal mean SST over

161 the two seas are depicted in Fig. 1. These regions are selected in such a way that the costal
162 influence on SST is eluded from the analysis. As the rainfall is scanty over the western AS
163 (west of 63°E latitude) during the ISM (Saikranthi et al. 2018), this region is also not
164 considered in the present analysis. The seasonal mean SST is higher over the BOB than in the
165 AS by more than 1 °C during the ISM season, in agreement with Shenoi et al. (2002). The
166 nearest space and time matched SST data from ERA-Interim are assigned to the TRMM-PR
167 and MODIS observations for further analysis.

168 **3. Variation of vertical structure of precipitation with SST**

169 The occurrence (in terms of %) of conditional precipitation echoes ($Z \geq 17$ dBZ) at
170 different altitudes as a function of SST over the AS and the BOB is shown in Fig. 2. The
171 variation of precipitation echo occurrence frequency with SST is quite different over both the
172 seas. The top of the precipitation echoes extends to higher altitudes with increasing SST over
173 the AS, while such variation is not quite evident over the BOB. Precipitation echoes are
174 confined to < 8 km at lower SST (< 28 °C) over the AS, but exhibits a gradual rise in height
175 with increase in SST. Large population density of precipitation echoes at lower altitudes is
176 mainly due to the abundant occurrence of shallow storms over the AS (Saikranthi et al. 2014;
177 Rao et al. 2016). Interestingly, the occurrence of precipitation echoes is seen at higher
178 altitudes even at lower SSTs over the BOB, indicating the presence of deeper storms. Such
179 systems exist at all SST's over the BOB.

180 To examine the variation of reflectivity profiles with SST, median profiles of
181 reflectivity in each SST bin are computed over the AS and the BOB separately for deep and
182 shallow systems and are depicted in Figs. 3 & 4, respectively. The space- and time-matched
183 conditional reflectivity profiles are grouped into 1°C SST bins and then the median is
184 estimated at each height, only if the number of conditional reflectivity pixels (Figs. 3c; 3f; 4c
185 & 4f) is greater than 500. The median reflectivity profiles corresponding to the deep systems

186 are distinctly different over the AS and the BOB (Figs. 3a & 3d), even at the same SST. Over
187 the AS, reflectivity of deep systems at different SSTs shows small variations (≤ 1 dBZ) above
188 the melting region (> 5 km), but varies significantly (~ 4.5 dBZ) below the melting level (< 5
189 km). These variations in reflectivity profiles with SST are negligible (< 0.5 dBZ) over the
190 BOB both above and below the melting region. The reflectivity increases from ~ 26.5 dBZ to
191 ~ 31 dBZ, with increase in SST from 26°C to 30°C over the AS, but it is almost the same (\sim
192 30 dBZ) at all SST's over the BOB below the melting layer. The standard deviation of
193 reflectivity, representing the variability in reflectivity within the SST bin, is similar at all
194 SSTs over both the seas except for the 26°C SST over AS. At this SST, the standard
195 deviation is lesser by ~ 1 dBZ than that of other SSTs.

196 The median reflectivity profiles of shallow storms depicted in Figs. 4a & 4d also
197 show a gradual increase in reflectivity from 20 dBZ to ~ 22 dBZ as SST changes from 26°C
198 to 31°C at the precipitation top altitude over the AS and don't show any variation with SST
199 over the BOB. However at 1 km altitude, except at 26°C SST over the AS, the reflectivity
200 variation with SST is not substantial over both the seas. The standard deviation of reflectivity
201 profiles show ~ 1 dBZ variation with SST (from 26°C to 31°C) at all altitudes over the AS
202 and don't show any variation over the BOB. The standard deviation of reflectivity for
203 shallow storms varies from 3 to 4 dBZ at the precipitation top altitude and 4.5 to 5.3 dBZ at 1
204 km altitude over the AS while it shows ~ 4 dBZ at precipitation top and ~ 5.5 dBZ at 1 km
205 altitude over the BOB.

206 **4. Factors affecting the vertical structure of precipitation and their variability with SST**

207 The formation and evolution of precipitating systems over oceans depend on dynamical,
208 thermodynamical and microphysical factors, like SST, wind shear, vertical wind velocity,
209 stability, CER, etc., and need to be considered for understanding the vertical structure of

210 precipitation (Li and Min 2010; reamean et al. 2013; Chen et al. 2015; Shige and Kummerov
211 2016; Guo et al 2018).

212 **4.1. Dynamical and thermodynamical factors:**

213 To understand the role of stability/instability, θ_e values computed from (1) using the
214 ERA-Interim datasets during the ISM period over the AS and the BOB are averaged for a
215 season and are depicted in Figs. 5(a) & 5(b), respectively. The surface θ_e (at 1000 hPa) values
216 are larger over the BOB than those over AS for the same SST, indicating that the instability
217 and convective available potential energy (CAPE) could be higher over the BOB. Indeed,
218 higher CAPE is seen over the BOB (Fig. S1, calculated following Emanuel 1994) than AS at
219 all SSTs by a magnitude $> 300 \text{ J kg}^{-1}$. The θ_e increases with SST from 358 °K to 368 °K
220 from 27 °C to 31 °C and from 350 °K to 363 °K from 26 °C to 31 °C over the BOB and the
221 AS, respectively. The CAPE also increases with rise in SST over both the seas. To know the
222 stability of the atmosphere θ_e gradients are considered. Irrespective of SST, positive gradients
223 in θ_e are observed between 900 and 800 hPa levels over the AS indicating the presence of
224 strong stable layers. The strength of these stable layers decreases with increasing SST. These
225 stable layers are formed mainly due to the flow of continental dry warm air from Arabian
226 Desert and Africa above the maritime air causing temperature inversions below 750 hPa level
227 over the AS during the ISM period (Narayanan and Rao 1981). However over the BOB, such
228 temperature inversions are not seen in the lower troposphere.

229 To understand the effect of wind field on the vertical structure of precipitation,
230 profiles of ISM seasonal mean vertical wind velocity and vertical shear in horizontal wind at
231 various SSTs over the AS and the BOB are shown in Figs. 5(c), 5(d) & 5(e), 5(f)
232 respectively. The updrafts are prevalent at all SSTs throughout the troposphere over the BOB,
233 whereas downdrafts are seen in the mid-troposphere (between 200 and 600 hPa levels) up to
234 27 °C and updrafts in the entire troposphere at higher SSTs over the AS. Also, the magnitude

235 of the vertical wind velocity varies significantly with SST in the mid-troposphere over the
236 AS. Over the BOB, the magnitude of updrafts increases with altitude in the lower and middle
237 troposphere, but doesn't vary much with SST. In the mid-troposphere, updrafts are stronger
238 by $> 0.02 \text{ Pa S}^{-1}$ over the BOB than over the AS. The profiles shown in Fig. 5(e) & 5(f) are
239 the mean vertical shear in horizontal wind estimated following Chen et al. (2015) at different
240 levels with reference to 950 hPa level. The wind shear increases with increasing altitude at all
241 the SSTs up to 400 hPa, but the rate of increase is distinctly different between the AS and the
242 BOB at SSTs less than $28 \text{ }^\circ\text{C}$ and nearly the same at higher SSTs. The wind shear decreases
243 systematically with SST ($\sim 1.5 \text{ m s}^{-1}$ for 1° increase in SST) in the middle troposphere over
244 the AS while the change is minimal over the BOB ($\sim 2 \text{ m s}^{-1}$ for $27 \text{ }^\circ\text{C}$ and $31 \text{ }^\circ\text{C}$).

245 Chen et al. (2015) highlighted the importance of mid-tropospheric wind shear in
246 generating mesoscale local circulations, like low-level cyclonic and upper-level anticyclonic
247 circulations. This feature is apparent over the AS, where down drafts are prevalent in mid-
248 upper troposphere and updrafts in the lower troposphere at lower SSTs. As SST increases, the
249 wind shear decreases and the updraft increases in the mid-troposphere. However, over the
250 BOB the wind shear is relatively weak when compared to the AS and hence the updrafts are
251 seen up to 200 hPa level at all SSTs. The weaker CAPE and stable mid-troposphere coupled
252 with upper- to mid- tropospheric downdrafts at lower SSTs over the AS inhibit the growth of
253 precipitating systems to higher altitudes and in turn precipitate in the form of shallow rain.
254 This result is in accordance with the findings of Shige and Kummerow (2016) that showed
255 the static stability at lower levels inhibits the growth of clouds and promotes the detrainment
256 of clouds over the Asian monsoon region and is considered as an important parameter in
257 determining the precipitation top height. As SST increases large CAPE and updrafts in the
258 middle troposphere collectively support the precipitating systems to grow to higher altitudes,
259 as evidenced in Fig. 2a. On the other hand, large CAPE and updrafts in the middle

260 troposphere prevalent over the BOB at all SSTs are conducive for the precipitating systems to
261 grow to higher altitudes as seen in Fig. 2b.

262 **4.2. Microphysical factors**

263 The observed differences in reflectivity profiles of precipitation with SST could be
264 originated at the cloud formation stage itself or manifested during the evolution stage or due
265 to both. Information on AOD and CER would be ideal to infer microphysical processes at the
266 cloud formation stage. CER values are mainly controlled by the ambient aerosols
267 concentration and the available moisture (Twomey 1977; Albrecht 1989; Tao et al. 2012; and
268 Rosenfeld et al. 2014). For fixed liquid water content, as the concentration of aerosols
269 increases, the number of cloud drops increases and CER decreases (Twomey 1977). To
270 understand the variation of AOD and TCWV and the resultant CER with SST, the mean
271 AOD and TCWV for different SST bins are plotted in Figs. 6a & 6b. The mean and standard
272 error are calculated only when the number of data points is more than 100 in each SST bin.
273 AOD decreases from 0.62 to 0.31 with rise in SST from 26 °C to 31 °C over the AS but only
274 from 0.42 to 0.36 as SST varies from 27 °C to 30 °C and then increases at higher SSTs over
275 the BOB. The variation of TCWV with SST (Fig. 6b) shows a gradual increase with SST
276 over the AS while it decreases initially from 27°C to 28°C, and then increases over the BOB.
277 At a given SST the TCWV is more in the BOB (> 8 mm) than in the AS.

278 The decrease in AOD and an increase in TCWV with SST result in an increase in
279 CER (14.7 μm to 20.8 μm from 26°C to 31°C) over the AS (Fig. 7). On the other hand, CER
280 doesn't show much variation with SST (18.5 μm to 19.5 μm from 27°C to 31°C) over BOB
281 due to smaller variations in AOD and TCWV. This also shows that the cloud droplets are
282 smaller in size at lower SSTs over the AS than BOB, while they are bigger and nearly equal
283 in size at higher SSTs. Since, reflectivity is more sensitive to the particle size ($Z \propto D^6$), the
284 smaller-sized hydrometeors at lower SSTs over the AS yield weaker reflectivity than over the

285 BOB (both for deep and shallow systems). As the SST increases, CER as well as the
286 reflectivity increases over the AS. At higher SSTs, the CER values are approximately equal
287 over both the seas and in turn the observed reflectivities (Figs. 3a & 4a). This suggests that
288 the variations seen in the reflectivity are originated in the cloud formation stage itself.

289 The hydrometeors also evolve during their descent to the ground due to several
290 microphysical processes. These processes can be inferred from the vertical structure of
291 precipitation or vertical profiles of reflectivity. The median reflectivity profiles of deep
292 systems show a gradual increase from ~ 10 km to 6 km and an abrupt enhancement is seen
293 just below 6 km over both the seas (Figs. 3a & 3d). The sudden enhancement at the freezing
294 level (radar bright band) is primarily due to the aggregation of hydrometeors and change in
295 dielectric factor from ice to water (Fabry and Zawadzki 1995; Rao et al. 2008; Cao et al.
296 2013). Below the bright band, raindrops grow by collision-coalescence process and reduce
297 their size by either breakup and/or evaporation processes. The collision-coalescence results in
298 negative slope in the reflectivity profile, whereas breakup and evaporation results in positive
299 slope (Liu and Zipser 2013; Cao et al. 2013; Saikranthi et al. 2014; Rao et al. 2016). The
300 observed negative slope ($\sim -0.3 \text{ dBZ km}^{-1}$) in the median reflectivity profiles below the
301 bright band indicates dominance of low-level hydrometeor growth over both the seas. The
302 magnitude of the slope decreases with SST over the AS, while it is nearly equal at all SSTs
303 over the BOB. It indicates the growth rate decreases with SST over the AS and remains the
304 same at all SSTs over the BOB. The median reflectivity profiles of shallow systems also
305 show negative slopes ($\sim -1 \text{ dBZ km}^{-1}$) at all SSTs representing the predominance of low-level
306 hydrometeor growth by collision-coalescence processes over both the seas.

307 The present analysis shows that the observed reflectivity changes with SST over both
308 the seas originate at the cloud formation stage and magnify further during the descent of
309 hydrometeors to ground.

310 **5. Conclusions**

311 Sixteen years of TRMM-PR 2A25 reflectivity profiles and 11 years of MODIS AOD
312 and CER data are utilized to understand the differences in variation of vertical structure of
313 precipitation with SST over AS and BOB. Precipitation top height increases with SST over
314 the AS indicating that systems grow to higher altitudes with increase in SST while it is almost
315 same at all SSTs representing that the systems are deeper over the BOB. The decrease in
316 stability and mid-tropospheric wind shear with SST over the AS favour the formation of
317 deeper system at higher systems. However the low stability and small wind shear at all SSTs
318 over the BOB help the formation of deeper systems. The variation of reflectivity with SST is
319 found to be remarkable over the AS and marginal over the BOB. The reflectivity increases
320 with rise in SST over the AS and remains the same at all SSTs over the BOB. This change in
321 reflectivity over the AS is more prominent below the freezing level height (~ 4 dBZ) than the
322 above (~ 1 dBZ). Over the AS, the abundance of aerosols and less moisture at SSTs $< 27^\circ\text{C}$
323 result in high concentration of smaller cloud droplets. As SST increases the aerosol
324 concentration decreases and moisture increases leading to the formation of bigger cloud
325 droplets. Thus, the reflectivity increases with rise in SST over the AS. On the other hand,
326 AOD, TCWV and CER do not show substantial variation with SST over the BOB and hence
327 the change in reflectivity is small. Over the BOB, the mid troposphere is wet and
328 hydrometeor's size at the formation stage is nearly the same at all SSTs. The evolution of
329 hydrometeors during their descent is also similar at all SST's. The collision-coalescence
330 process is predominant below the bright band region over both the seas and is responsible for
331 the observed negative slope in the reflectivity profiles.

332 **Author contributions**

333 Kadiri Saikranthi conceived the idea. Kadiri Saikranthi and Basivi Radhakrishna designed the
334 analysis, plotted the figures and wrote the manuscript. Thota Narayana Rao and Sreedharan

335 Krishnakumari Satheesh contributed in discussions and also in writing the manuscript.

336 **Acknowledgements**

337 The authors would like to thank Prof. Robert Houze and his team for the interpolated 3D
338 gridded TRMM-PR dataset (<http://trmm.atmos.washington.edu>), ECMWF (<http://data-portal.ecmwf.int/>) team for providing the ERA-Interim dataset and MODIS
339 (<https://ladsweb.modaps.eosdis.nasa.gov/>) science team for providing the AOD and CER
340 dataset. The authors express their gratitude to Prof. J. Srinivasan for his fruitful discussions
341 and valuable suggestions in improving the quality of the manuscript. The corresponding
342 author would like to thank Department of Science & Technology (DST), India for providing
343 the financial support through the reference number DST/INSPIRE/04/2017/001185. We
344 thank the two referees for their critical comments in improving the quality of the manuscript.

346 **References**

- 347 Albrecht, B.A.: Aerosols, cloud microphysics, and fractional cloudiness, *Science*, 245, 1227–
348 1230, 1989.
- 349 Awaka, J., Iguchi, T., and Okamoto, K.: TRMM PR standard algorithm 2A23 and its
350 performance on bright band detection, *J. Meteorol. Soc. Jpn.*, 87A, 31–52, 2009.
- 351 Bhat, G. S., Gadgil, S., Kumar, P. V. H., Kalsi, S. R., Madhusoodanan, P., Murty, V. S., Rao,
352 C. V. P., Babu, V. R., Rao, L.V., Rao, R. R., Ravichandran, M., Reddy, K.G., Rao, P.
353 S., Sengupta, D., Sikka, D. R., Swain, J., and Vinayachandran, P. N.: BOBMEX: The
354 Bay of Bengal Monsoon Experiment, *Bull. Amer. Meteor. Soc.*, 82, 2217–2244, 2001.
- 355 Cao, Q., Hong, Y., Gourley, J. J., Qi, Y., Zhang, J., Wen, Y., and Kirstetter, P. E.: Statistical
356 and physical analysis of the vertical structure of precipitation in the mountainous west
357 region of the United States using 11+ years of space borne observations from TRMM
358 precipitation radar, *J. Appl. Meteorol. Climatol.*, 52, 408-424, 2013.

- 359 Chaudhari, H. S., Pokhrel, S., Kulkarni, A., Hazra, A., and Saha, S. K.: Clouds-SST
360 relationship and interannual variability modes of Indian summer monsoon in the
361 context of clouds and SSTs: observational and modelling aspects, *Int. J. Climatol.*, doi:
362 10.1002/joc.4664, 2016.
- 363 Chaudhari, H. S., Pokhrel, S., Mohanty, S., and Saha, S. K.: Seasonal prediction of Indian
364 summer monsoon in NCEP coupled and uncoupled model, *Theor. Appl. Climatol.*, 114,
365 459–477, doi:10.1007/s00704-013-0854-8, 2013.
- 366 Chen, Q., Fan, J., Hagos, S., Gustafson Jr., W. I., and Berg, L. K.: Roles of wind shear at
367 different vertical levels: Cloud system organization and properties, *J. Geophys. Res.*
368 *Atmos.*, 120, 6551–6574, 2015.
- 369 Creamean, J. M., Suski, K. J., Rosenfeld, D., Cazorla, A., DeMott, P. J., Sullivan, R. C.,
370 White, A. B., Ralph, F. M., Minnis, P., Comstock, J. M., Tomlinson, J. M., Kimberly
371 A., and Prather, K. A.: Dust and biological aerosols from the Sahara and Asia influence
372 precipitation in the western U.S., *Science*, 339, 1572–1578,
373 doi:10.1126/science.1227279, 2013.
- 374 Dee, D. P., et al.: The ERA-Interim reanalysis: Configuration and performance of the data
375 assimilation system, *Q. J. R. Meteorol. Soc.*, 137, 553–597, 2011.
- 376 Emanuel, K. A.: Atmospheric convection. Oxford University Press, Oxford, 1994.
- 377 Fabry, F., and Zawadzki, I.: Long-term radar observations of the melting layer of
378 precipitation and their interpretation, *J. Atmos. Sci.*, 52, 838–851, 1995.
- 379 Feng, X., Haines, K., Liu, C., de Boissésou, E., and Polo, I., Improved SST-precipitation
380 intraseasonal relationships in the ECMWF coupled climate reanalysis, *Geophys. Res.*
381 *Lett.*, 45, 3664–3672, 2018.
- 382 Findlater, J.: A major low-level air current near the Indian Ocean during the northern
383 summer, *Q. J. R. Meteorol. Soc.*, 95, 362–380, 1969.

- 384 Fu, Y., and Liu, G.: The variability of tropical precipitation profiles and its impact on
385 microwave brightness temperatures as inferred from TRMM data, *J. Appl. Meteorol.*,
386 40, 2130–2143, 2001.
- 387 Gadgil, S., Joseph, P. V., and Joshi, N. V.: Ocean atmosphere coupling over monsoonal
388 regions, *Nature*, 312, 141-143, 1984.
- 389 Gadgil, S.: Monsoon–ocean coupling. *Current Sci.*, 78, 309–323, 2000.
- 390 Geerts, B., and Dejene, T.: Regional and diurnal variability of the vertical structure of
391 precipitation systems in Africa based on space borne radar data, *J. Clim.*, 18, 893–916,
392 2005.
- 393 Guo, J., Liu, H., Li, Z., Rosenfeld, D., Jiang, M., Xu, W., Jiang, J. H., He, J., Chen, D., Min,
394 M., and Zhai, P.: Aerosol-induced changes in the vertical structure of precipitation: a
395 perspective of TRMM precipitation radar, *Atmos. Chem. Phys.*, 18, 13329-13343,
396 <https://doi.org/10.5194/acp-18-13329-2018>, 2018.
- 397 Houze, R. A., and Churchill, D. D.: Mesoscale organization and cloud microphysics in a Bay
398 of Bengal depression, *J. Atmos. Sci.*, 44, 1845–1867, 1987.
- 399 Houze, R. A., Rasmussen, K. L., Zuluaga, M. D., and Brodzik, S. R.: The variable nature of
400 convection in the tropics and subtropics: A legacy of 16 years of the Tropical rainfall
401 measuring mission satellite, *Rev. Geophys.*, 53, 994–1021, 2015.
- 402 Houze, R. A., Wilton, D. C., and Smull, B. F.: Monsoon convection in the Himalayan region
403 as seen by the TRMM precipitation radar, *Q. J. R. Meteorol. Soc.*, 133, 1389-1411,
404 2007.
- 405 Houze, R. A.: Mesoscale convective systems, *Rev. Geophys.*, 42, RG4003, doi:
406 10.1029/2004RG000150, 2004.
- 407 Hsu, N., Tsay, S., King, M., and Herman, J.: Aerosol properties over bright-reflecting source
408 regions, *Geosci. Remote Sens. IEEE Trans.*, 42, 557–569, 2004.

- 409 Hubanks, P., King, M., Platnick, S., and Pincus, R.: MODIS atmosphere L3 gridded product
410 algorithm theoretical basis document collection 005 Version 1.1, Tech. Rep. ATBD-
411 MOD-30, NASA, 2008.
- 412 Iguchi, T., Kozu, T., Kwiatkowski, J., Meneghini, R., Awaka, J., and Okamoto, K.:
413 Uncertainties in the rain profiling algorithm for the TRMM precipitation radar, *J.*
414 *Meteor. Soc. Japan*, 87A, 1–30, doi:10.2151/jmsj.87A.1, 2009.
- 415 Krishnamurti, T. N.: Summer monsoon experiment – A review. *Mon. Wea. Rev.*, 113, 1590-
416 1626, 1985.
- 417 Krishnamurti, T.: Cooling of the Arabian Sea and the onset-vortex during 1979. Recent
418 progress in equatorial oceanography: A report of the final meeting of SCOR
419 WORKING GROUP 47 in Venice, Italy, 1-12, 1981. [Available from Nova Univ.,
420 Ocean Science Center, Dania, FL 33004].
- 421 Levy, R., Remer, L., Mattoo, S., Vermote, E., and Kaufman, Y.: Second-generation
422 operational algorithm: Retrieval of aerosol properties over land from inversion of
423 moderate resolution imaging spectroradiometer spectral reflectance, *J. Geophys. Res.*,
424 112, D13, doi:10.1029/2006JD007811, 2007.
- 425 Li, R., and Min, Q.-L.: Impacts of mineral dust on the vertical structure of precipitation. *J.*
426 *Geophys. Res.*, 115, D09203, doi:10.1029/2009JD011925, 2010.
- 427 Liu, C., Zipser, E., and Nesbitt, S. W.: Global distribution of tropical deep convection:
428 Different perspectives using infrared and radar as the primary data source, *J. Climate*,
429 20, 489-503, 2007.
- 430 Liu, C., and Zipser, E. J.: Why does radar reflectivity tend to increase downward toward the
431 ocean surface, but decrease downward toward the land surface?, *J. Geophys. Res.*
432 *Atmos.*, 118, 135-148, doi: 10.1029/2012JD018134, 2013.

- 433 Meenu, S., Parameswaran, K., and Rajeev, K.: Role of sea surface temperature and wind
434 convergence in regulating convection over the tropical Indian Ocean, *J. Geophys. Res.*
435 *Atmos.*, 117, D14102, 2012.
- 436 Nair, A. K. M., and Rajeev, K.: Multiyear CloudSat and CALIPSO observations of the
437 dependence of cloud vertical distribution on sea surface temperature and tropospheric
438 dynamics, *J. Clim.*, 27, 672–683, doi:10.1175/JCLI-D-13-00062.1, 2014.
- 439 Narayanan, M. S., and Rao, B. M.: Detection of monsoon inversion by TIROS-N satellite,
440 *Nature*, 294, 546-548, 1981.
- 441 Nuijens, L., Emanuel, K., Masunaga, H., and L'Ecuyer, T.: Implications of warm rain in
442 shallow cumulus and congestus clouds for large-scale circulations, *Surv. Geophys.*, 38,
443 1257-1282, 2017.
- 444 Oueslati, B., and Bellon, G.: The double ITCZ bias in CMIP5 models: interaction between
445 SST, large-scale circulation and precipitation. *Clim. Dyn.*, 44, 585-607, 2015.
- 446 Platnick, S., et al.: The MODIS cloud optical and microphysical products: Collection 6
447 updates and examples from Terra and Aqua, *IEEE Trans. Geosci. Remote Sens.*, 55,
448 502–525, doi:10.1109/TGRS.2016.2610522, 2017.
- 449 Rajeevan, M., Unnikrishnan, C. K., and Preethi, B.: Evaluation of the ENSEMBLES multi-
450 model seasonal forecasts of Indian summer monsoon variability, *Clim. Dyn.*, 38, 2257–
451 2274, 2012.
- 452 Rajendran, K., Nanjundiah, R. S., Gadgil, S., and Srinivasan, J.: How good are the
453 simulations of tropical SST–rainfall relationship by IPCC AR4 atmospheric and
454 coupled models?, *J. Earth Sys. Sci.*, 121(3), 595–610, 2012.
- 455 Rao, T. N., Kirankumar, N. V. P., Radhakrishna, B., Rao, D. N., and Nakamura, K.:
456 Classification of tropical precipitating systems using wind profiler spectral moments.

- 457 Part I: Algorithm description and validation, *J. Atmos. Oceanic Technol.*, 25, 884–897,
458 2008.
- 459 Rao, T. N., Saikranthi, K., Radhakrishna, B., and Rao, S. V. B.: Differences in the
460 climatological characteristics of precipitation between active and break spells of the
461 Indian summer monsoon, *J. Clim.*, 29, 7797-7814, 2016.
- 462 Remer, L., Kaufman, Y., Tanré, D., Mattoo, S., Chu, D., Martins, J., Li, R., Ichoku, C.,
463 Levy, R., Kleidman, R., Eck, T., Vermote, E., and Holben, B.: The MODIS aerosol
464 algorithm, products, and validation, *J. Atmos. Sci.*, 62, 947–973, 2005.
- 465 Romatschke, U., Medina, S., and Houze, R. A.: Regional, seasonal, and diurnal variations of
466 extreme convection in the South Asian region, *J. Clim.*, 23, 419–439, 2010.
- 467 Rosenfeld, D., et al.: Global observations of aerosol-cloud-precipitation-climate interactions,
468 *Rev. Geophys.*, 52, 750-808, doi:10.1002/2013RG000441, 2014.
- 469 Roxy, M., Tanimoto, Y., Preethi, B., Terray, P., and Krishnan, R.: Intraseasonal SST-
470 precipitation relationship and its spatial variability over the tropical summer monsoon
471 region, *Clim. Dyn.*, 41, 45-61, 2013.
- 472 Roxy, M.: Sensitivity of precipitation to sea surface temperature over the tropical summer
473 monsoon region—and its quantification, *Clim. Dyn.*, 43, 1159-1169, 2014.
- 474 Sabin, T., Babu, C., and Joseph, P.: SST–convection relation over tropical oceans, *Int. J.*
475 *Climatol.* 33, 1424–1435, 2012.
- 476 Saikranthi, K., Radhakrishna, B., Satheesh, S. K., and Rao, T. N.: Spatial variation of
477 different rain systems during El Niño and La Niña periods over India and adjoining
478 ocean, *Clim. Dyn.*, 50, 3671-3685, doi: 10.1007/s00382-017-3833-4, 2018.
- 479 Saikranthi, K., Rao, T. N., Radhakrishna, B., and Rao, S. V. B. : Morphology of the vertical
480 structure of precipitation over India and adjoining oceans based on long-term

- 481 measurements of TRMMPR, *J. Geophys. Res. Atmos.*, 119, 8433–8449, doi:
482 10.1002/2014JD021774, 2014.
- 483 Sathiyamoorthy, V., Mahesh, C., Gopalan, K., Prakash, S., Shukla, B. P., Mathur, A.:
484 Characteristics of low clouds over the Arabian Sea, *J. Geophys. Res. Atmos.*, 118,
485 13489-13503, 2013.
- 486 Schumacher, C. and Houze, R. A.: Stratiform rain in the tropics as seen by the TRMM
487 precipitation radar, *J. Climate.*, 16, 1739–1756, 2003.
- 488 Sengupta, D., Goswami, B. N., and Senan, R.: Coherent intraseasonal oscillations of ocean
489 and atmosphere during the Asian summer monsoon, *Geophys. Res. Lett.*, 28, 4127–
490 4130, 2001.
- 491 Shenoi, S. S. C., Shankar, D., and Shetye, S. R.: Differences in heat budgets of the near-
492 surface Arabian Sea and Bay of Bengal: Implications for the summer monsoon, *J.*
493 *Geophys. Res.*, 107(C6), 3052, doi:10.1029/2000JC000679, 2002.
- 494 Shige, S. and Kummerow, C.D.: Precipitation-Top Heights of Heavy Orographic Rainfall in
495 the Asian Monsoon Region, *J. Atmos. Sci.*, 73, 3009–3024, 2016.
- 496 Sunilkumar, K., Rao, T. N., Saikranthi, K., and Rao, M. P.: comprehensive evaluation of
497 multisatellite precipitation estimates over India using gridded rainfall data, *J. Geophys.*
498 *Res. Atmos.*, 120, doi:10.1002/2015JD023437, 2015.
- 499 Takayabu, Y. N., Shige, S., Tao, W., and Hirota, N.: Shallow and deep latent heating modes
500 over tropical Oceans observed with TRMM PR spectral latent heating Data, *J. Climate*,
501 23, 2030–2046, 2010.
- 502 Tao, W.-K., Chen, J.-P., Li, Z., Wang, C., and Zhang, C.: Impact of aerosols on convective
503 clouds and precipitation, *Rev. Geophys.*, 50, RG2001, doi:10.1029/2011RG000369,
504 2012.

- 505 Tao, W.-K., et al.: Retrieval of latent heating from TRMM measurements, *Bull. Am.*
506 *Meteorol. Soc.*, 87, 1555–1572, 2006.
- 507 Twomey, S.: The influence of pollution on the short wave albedo of clouds, *J. Atmos. Sci.*,
508 34, 1149–1152, 1977.
- 509 Wallace, J. M., and Hobbs, P. V.: Atmospheric science: An introductory survey, Second
510 edition, Academic press, pp. 85, 2006.
- 511 Wang, B., Ding, Q., Fu, X., Kang, I.-S., Jin, K., Shukla, J., and Doblas-Reyes, F.:
512 Fundamental challenge in simulation and prediction of summer monsoon rainfall,
513 *Geophys. Res. Lett.*, 32, L15711, doi:10.1029/2005GL022734, 2005.
- 514 Weller, R. A., Farrar, J. T., Buckley, J., Mathew, S., Venkatesan, R., Lekha, J. S., Chaudhuri,
515 D., Kumar, N. S., and Kumar, B. P.: Air-sea interaction in the Bay of Bengal,
516 *Oceanography*, 29(2), 28–37, 2016.
- 517 Woolnough, S.J., Slingo, J.M., and Hoskins, B.J.: The relationship between convection and
518 sea surface temperature on intraseasonal timescales, *J. Climate*, 13, 2086–2104, 2000.
- 519 Wu, R., and Kirtman, B. P.: Roles of Indian and Pacific Ocean air–sea coupling in tropical
520 atmospheric variability, *Clim. Dyn.*, 25(2–3), 155–170, 2005.

521

522

523

524

525

526

527

528

529

Figure captions

530
531
532
533
534
535
536
537
538
539
540
541
542
543
544
545
546
547
548
549
550
551
552
553
554
555

Figure 1: Spatial distribution of ISM mean SST (in °C) obtained from ERA-Interim reanalysis data over the AS (63°E-72°E & 8°N-20°N) and the BOB (83°E-92°E & 8°N-21°N). The regions considered in this analysis over these two seas are shown with the boxes.

Figure 2: (a) and (b) represent the altitudinal distribution of occurrence of conditional reflectivity (≥ 17 dBZ) as a function of SST with respect to precipitation occurrence at that particular SST interval over the AS and the BOB, respectively.

Figure 3: (a), (d) and (b), (e) represent vertical profiles of median reflectivity correspond to deep systems and their standard deviation (in dBZ) with SST over the AS and the BOB, respectively during the ISM season. (c) and (f) show the number of conditional reflectivity pixels at each altitude used for the estimation of the median and standard deviation.

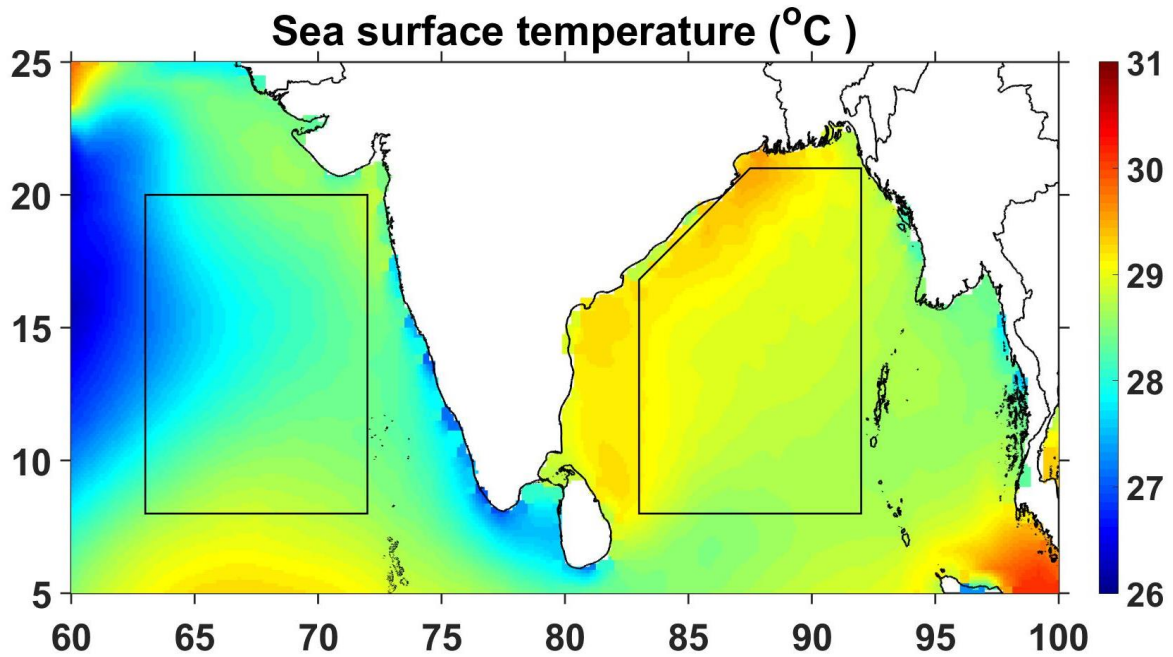
Figure 4: Same as Fig. 3 but for shallow precipitating systems.

Figure 5: (a) and (b), respectively, represent the vertical profiles of mean θ_e (in K) with SST over the AS and the BOB during the ISM season. (c) and (d) and (e) and (f) are same as (a) and (b) but for mean vertical velocity (in Pa s^{-1}) and wind gradient with reference to 950 hPa level (in m s^{-1}).

Figure 6: (a) Mean and standard error of AOD and (b) TCWV (in mm) with SST over the AS and the BOB during ISM.

Figure 7: Variation of mean and standard error of CER liquid (in μm) with SST over the AS and the BOB during the ISM season.

Figures



558

559 **Figure 1:** Spatial distribution of ISM mean SST (in °C) obtained from ERA-Interim
560 reanalysis data over the AS (63°E-72°E & 8°N-20°N) and the BOB (83°E-92°E &
561 8°N-21°N). The regions considered in this analysis over these two seas are shown
562 with the boxes.

563

564

565

566

567

568

569

570

571

572

573

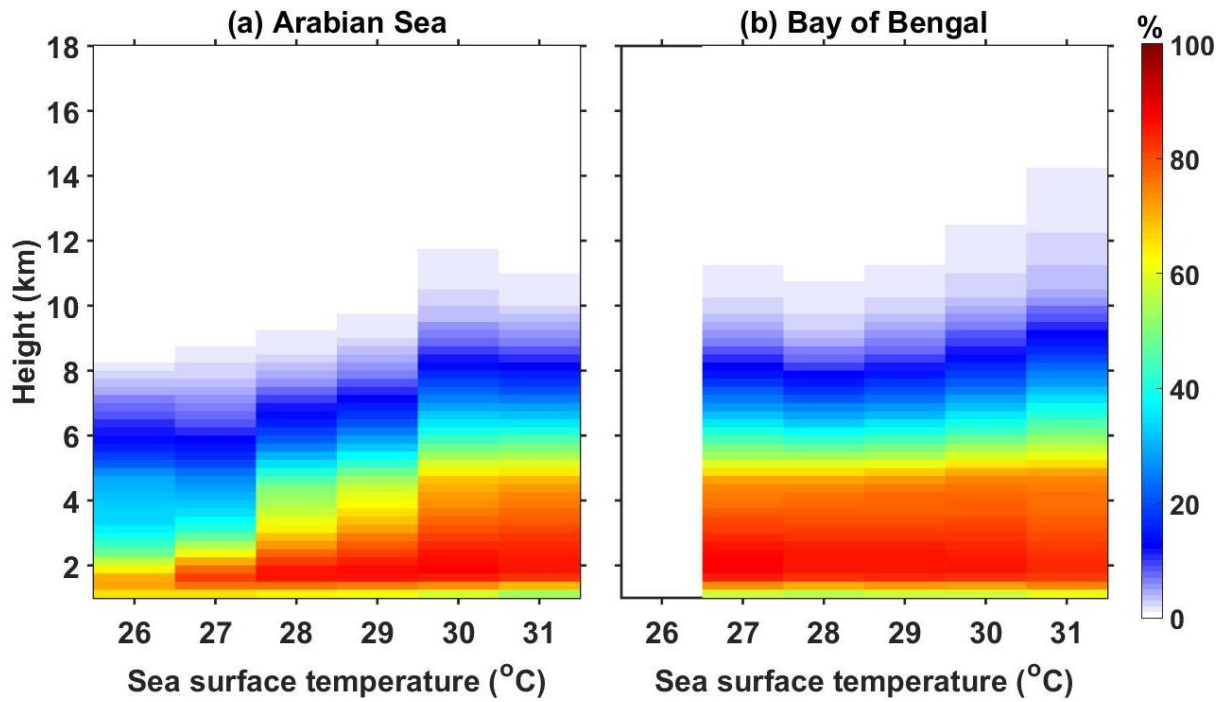
574

575

576

577

578



579

580

581 **Figure 2:** (a) and (b) represent the altitudinal distribution of occurrence of conditional
 582 reflectivity (≥ 17 dBZ) as a function of SST with respect to precipitation occurrence at
 583 that particular SST interval over the AS and the BOB, respectively.

584

585

586

587

588

589

590

591

592

593

594

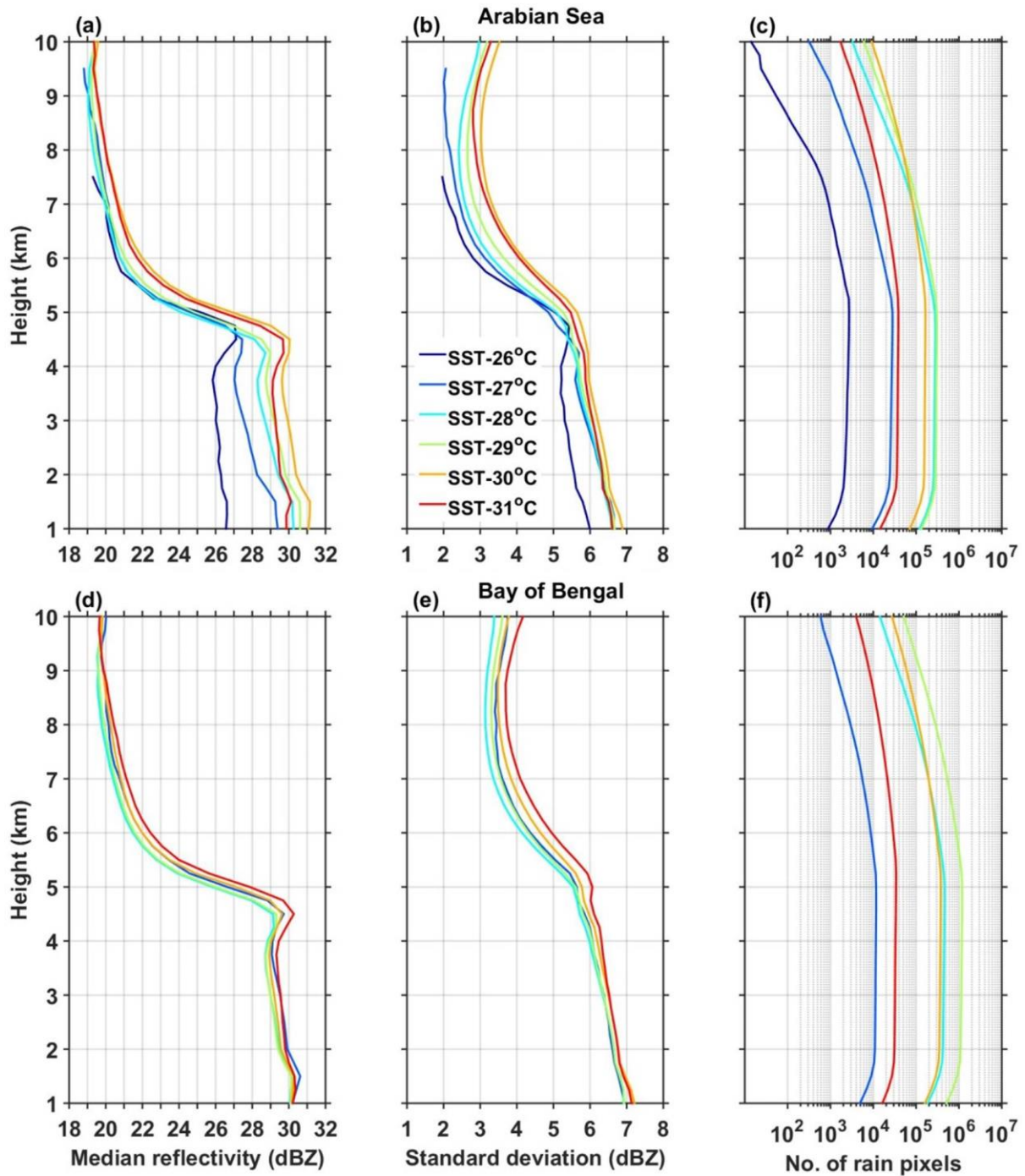
595

596

597

598

599



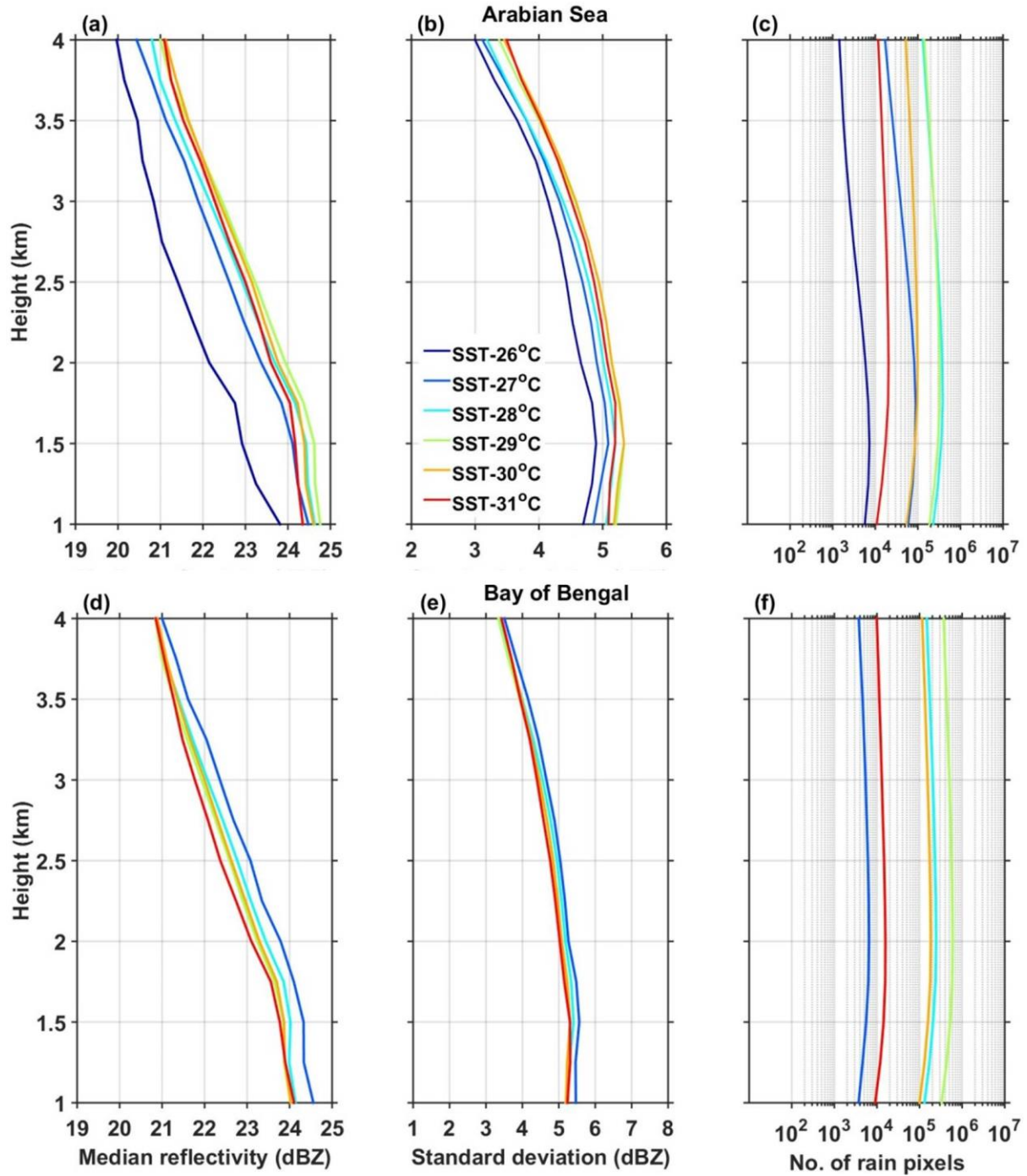
600

601 **Figure 3:** (a), (d) and (b), (e) represent vertical profiles of median reflectivity correspond to
 602 deep systems and their standard deviation (in dBZ) with SST over the AS and the
 603 BOB, respectively during the ISM season. (c) and (f) show the number of conditional
 604 reflectivity pixels at each altitude used for the estimation of the median and
 605 standard deviation.

606

607

608



609

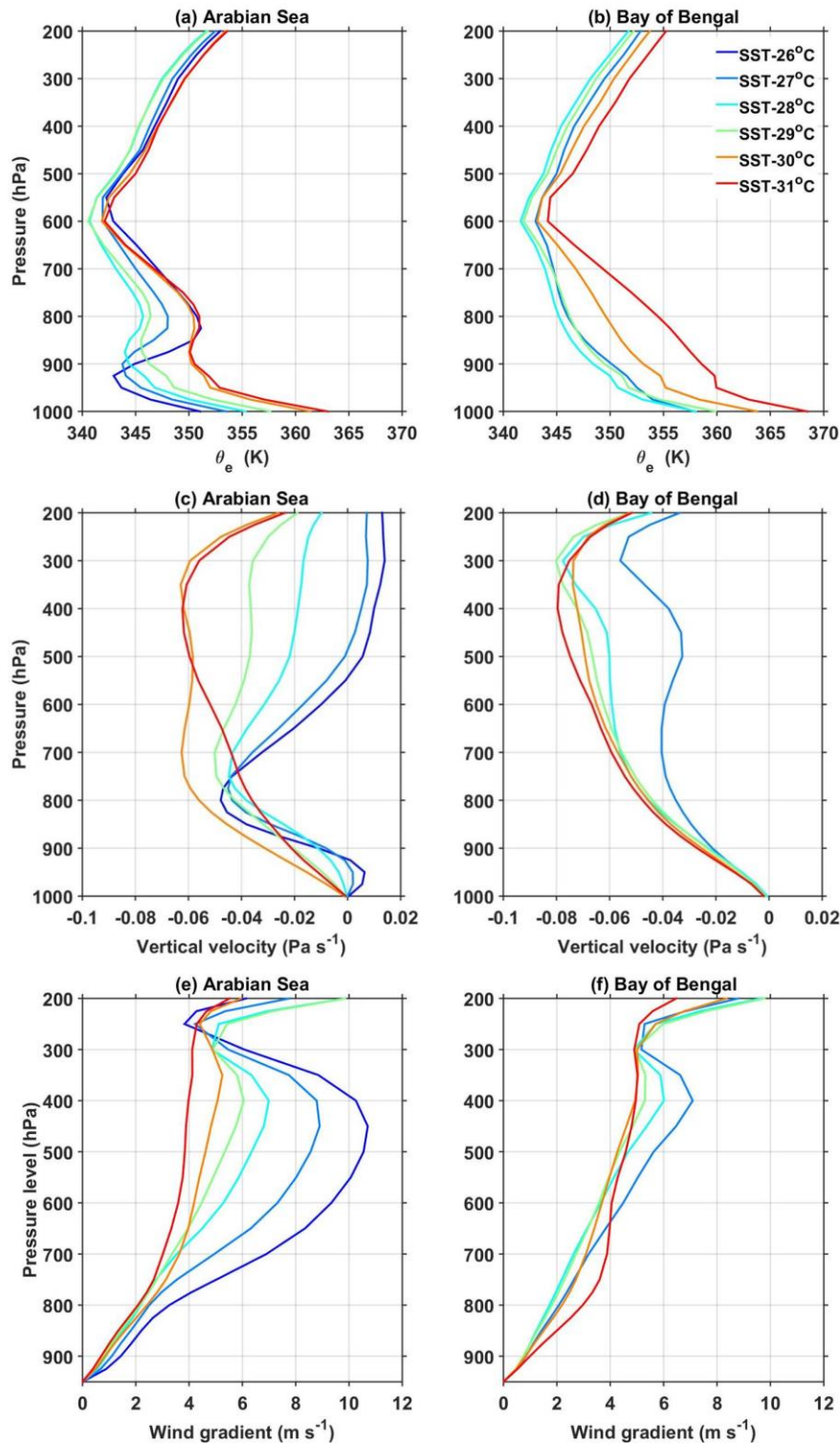
610 **Figure 4:** Same as Fig. 3 but for shallow precipitating systems.

611

612

613

614
 615
 616
 617
 618
 619
 620
 621
 622
 623
 624
 625
 626
 627
 628
 629
 630
 631
 632
 633
 634
 635
 636
 637
 638
 639
 640



641 **Figure 5:** (a) and (b), respectively, represent the vertical profiles of mean θ_e (in K) with SST
 642 over the AS and the BOB during the ISM season. (c) and (d) and (e) and (f) are same
 643 as (a) and (b) but for mean vertical velocity (in Pa s^{-1}) and wind gradient with
 644 reference to 950 hPa level (in m s^{-1}).

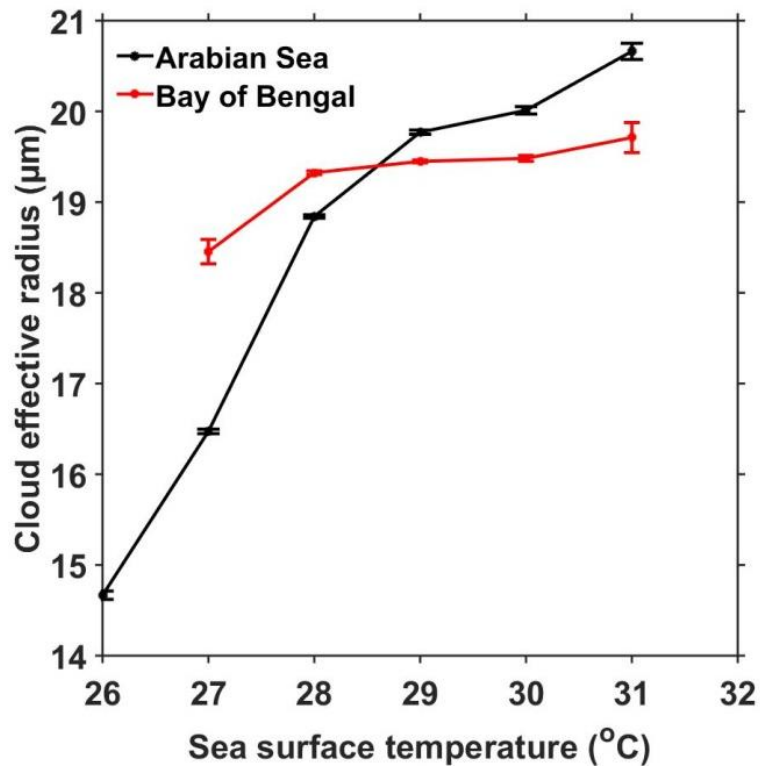


Figure 6: Variation of mean and standard error of CER liquid (in μm) with SST over the AS and the BOB during the ISM season.

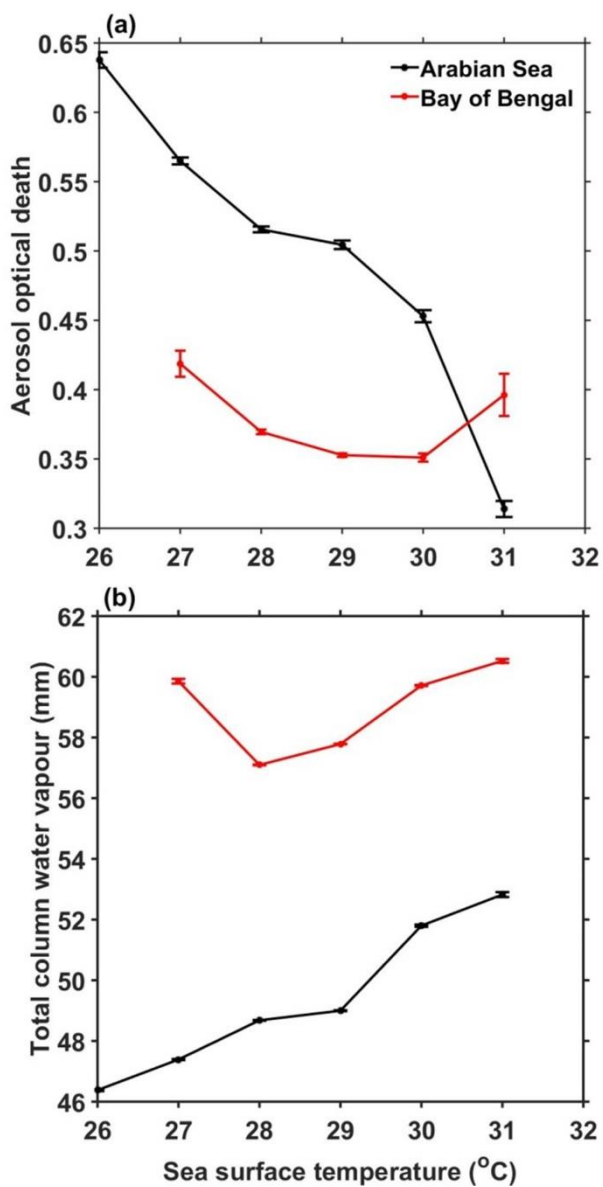


Figure 7: (a) Mean and standard error of AOD and (b) TCWV (in mm) with SST over the AS and the BOB during ISM.

Supplementary material

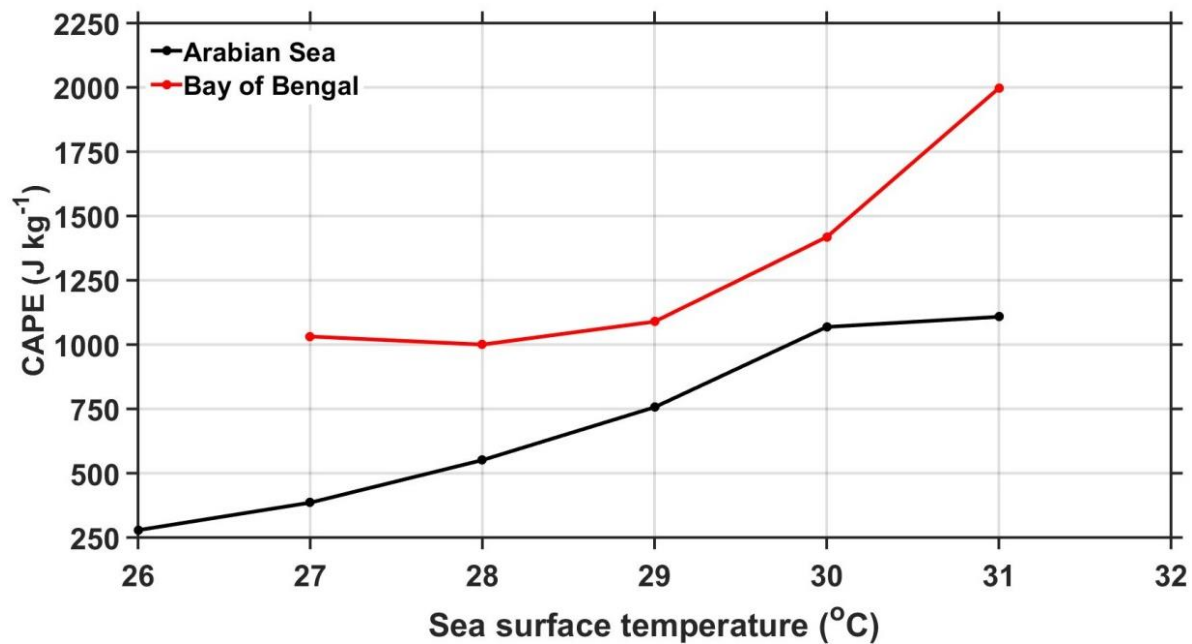
706
707
708
709
710
711
712
713
714
715
716
717
718
719
720
721
722
723
724
725
726
727
728
729
730
731

Satheesh et al. (2006) showed an increase in AOD with increase in latitude over the AS due to the dust advection from Arabia desert regions during ISM season, whereas SST decreases with increase in the latitude. In other words the SST is low and AOD is high in northern AS whereas over the southern AS, SST is high and AOD is low. This contrasting spatial distribution of AOD and SST could cause a negative correlation between AOD and SST as depicted in Fig. 6a. To examine whether the observed decrease in AOD with increase in SST over the AS is due to the latitudinal variation of AOD or exists at all latitudes, we have segregated the data into 2° latitude bins and plotted the mean AOD with SST for all bins and is depicted in Fig. S2. In spite of the magnitude, AOD variation with SST is nearly similar at all latitudes of the AS, i.e., the higher AOD is observed at lower SSTs and vice versa (Fig. S2a). On the other hand the latitudinal variation of AOD with SST over the BOB shown in Fig. S2b also show a decrease in AOD with SST till 30 °C but the magnitude of variation is trivial relative to the AS. Also, as depicted in Fig. 6a AOD increases above 30 °C with SST over the BOB. This indicates that though there is a difference in magnitude of variation, AOD varies with SST over both the seas at all latitudes. This analysis is repeated using the multi-angle imaging spectroradiometer (MISR) dataset (which is not shown here) for small, medium large aerosol particles. Interestingly all three types also show a decrease in AOD with rise in SST over both the seas.

Satheesh, S. K., Moorthy, K. K., Kaufman, Y. J., and Takemura, T.: Aerosol Optical depth, physical properties and radiative forcing over the Arabian Sea, *Meteorol. Atmos. Phys.*, 91, 45–62, doi:10.1007/s00703-004-0097-4, 2006.

732

733



734

735 **Figure S1:** Variation of mean CAPE (in J kg⁻¹) with SST over the AS and the BOB during
736 the ISM season.

737

738

739

740

741

742

743

744

745

746

747

748

749

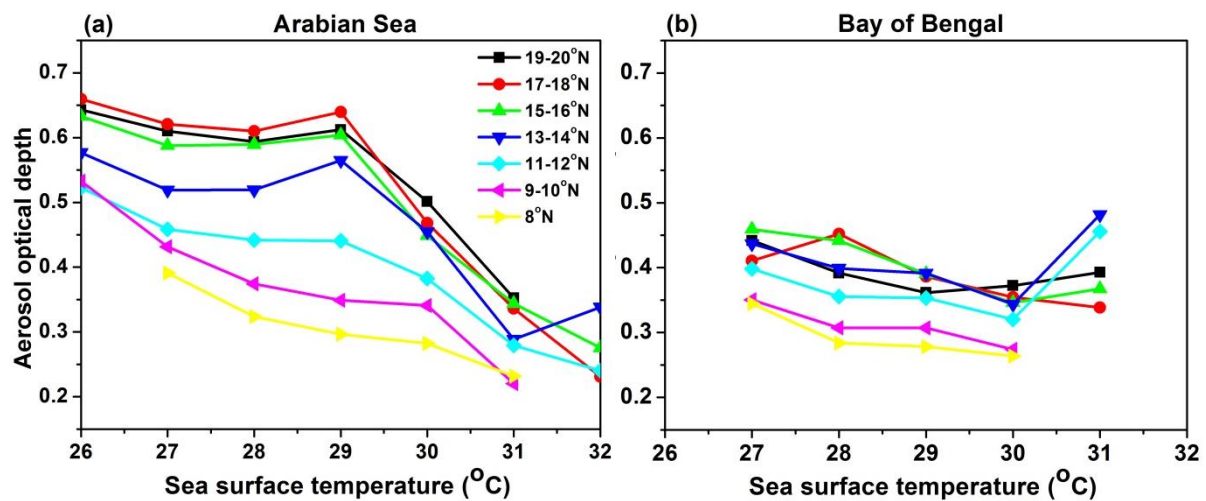
750

751

752

753

754



755

756 **Figure S2:** (a) and (b), respectively, represent latitudinal variation (for every 2 $^{\circ}$ latitude
 757 interval) of mean AOD over the AS (between 63 $^{\circ}\text{E}$ and 72 $^{\circ}\text{E}$) and the BOB (between
 758 83 $^{\circ}\text{E}$ and 92 $^{\circ}\text{E}$).